



# Numerical Studies on the Effects of Stagnation Pressure and Temperature on Supersonic Flow Characteristics in Cold Spray Applications

Min-Wook Lee, Jung-Jae Park, Do-Yeon Kim, Sam S. Yoon, Ho-Young Kim, Scott C. James, Sanjeev Chandra, and Thomas Coyle

(Submitted August 30, 2010; in revised form January 24, 2011)

Low-temperature particle coating requires supersonic flow. The characteristics of this supersonic flow are investigated using a nonlinear turbulence model. The low-temperature, supersonic particle deposition technique is valuable because its rapid and dense coating minimizes thermal damage to both particles and substrate. It has excellent potential for industrial production of low-cost thin films. Stagnation pressures and temperatures of the supersonic nozzle range from  $4 < P_o < 45$  bar and  $300 < T_o < 1500$  K, respectively. The exit Mach number,  $M_e$ , and velocity,  $V_e$ , range from 0.6 to 3.5 and 200 to 1400 m/s, respectively. The effects of stagnation pressure ( $P_o$ ) and stagnation temperature ( $T_o$ ) on supersonic flow impinging upon a substrate are described. In other words, the energy loss through shockwaves and shear interactions between the streaming jet and surrounding gas are quantified as functions of  $P_o$  and  $T_o$ .  $P_o$  is decreased because of friction (loss ranges from 40 to 60%) while  $T_o$  is nearly conserved. To realize the nozzle exit condition of  $P_e = P_{amb}$ , we demonstrate that  $P_o$  should be adjusted rather than  $T_o$ , as  $T_o$  has little effect on exit pressures. On the other hand,  $T_o$  is more influential than  $P_o$  for varying the exit velocity. Various nozzle geometries yielding different flow characteristics, and hence, different operating conditions and coating performances are investigated. The corresponding supersonic flows for three types of nozzles (under-, correctly, and over-expanded) are simulated, and their correctly expanded (or shock-free) operating conditions are identified. Diamond shock structures induced by the pressure imbalance between the exiting gas and the surrounding atmosphere are captured.

**Keywords** cold spray, diamond shock structure, supersonic nozzle, thin-film coating

## 1. Introduction

Cold spray (Ref 1-4) is an attractive deposition technique because it does not require heating of the working fluid by plasma or substrate as do thermal spray coating techniques (Ref 5). The proposed relatively low-temperature process has advantages, over other techniques, such as energy saving and prevention of thermal damage to the coating materials and substrates.

As shown in Fig. 1, gas is supplied through a converging-diverging *de Laval* nozzle that accelerates the flow to

supersonic. Particles may be injected into the flow, which eventually stagnates at the substrate where, upon collision, they are pulverized, spread, and deposited through a rapid thermal-and-cooling bonding process (Ref 1). Particles (the coating material) are typically polymers, metals, composites, or ceramics and are used for thermal barrier coatings, corrosion protection (Ref 6), or electronic-display components like micro-actuators and high-speed optical modulators (Ref 7). Fundamental flow physics of cold sprays were studied by Jodoin (Ref 8), and experimental data are available for many materials such as copper (Ref 1, 3, 4, 9), aluminum (Ref 4, 10-12), titanium (Ref 13), and nickel-based alloys (Ref 14). There are numerous numerical studies on cold spray techniques as well (Ref 15-17).

In an industrial coating process, the coating engineer generally has limited ability to optimize the supersonic flow, which is typically controlled by the operating (or stagnation) pressure and temperature. Typically, trial-and-error is used; if the desired particle speed is not attained, then the engineer increases the pressure and temperature (often leading to over-specified operating conditions). Even when the coating is successful, the engineer is still unaware of the resulting supersonic flow conditions. Clearly, an informed approach to supersonic flow characterization is preferable.

Min-Wook Lee, Jung-Jae Park, Do-Yeon Kim, Sam S. Yoon, and Ho-Young Kim, Department of Mechanical Engineering, Korea University, Seoul 136-713, Korea; Scott C. James, Thermal/Fluid Science & Engineering, Sandia National Laboratories, Livermore, CA; and Sanjeev Chandra and Thomas Coyle, Department of Mechanical and Industrial Engineering, University of Toronto, 5 King's College Road, Toronto, ON, Canada. Contact e-mail: skyoon@korea.ac.kr.

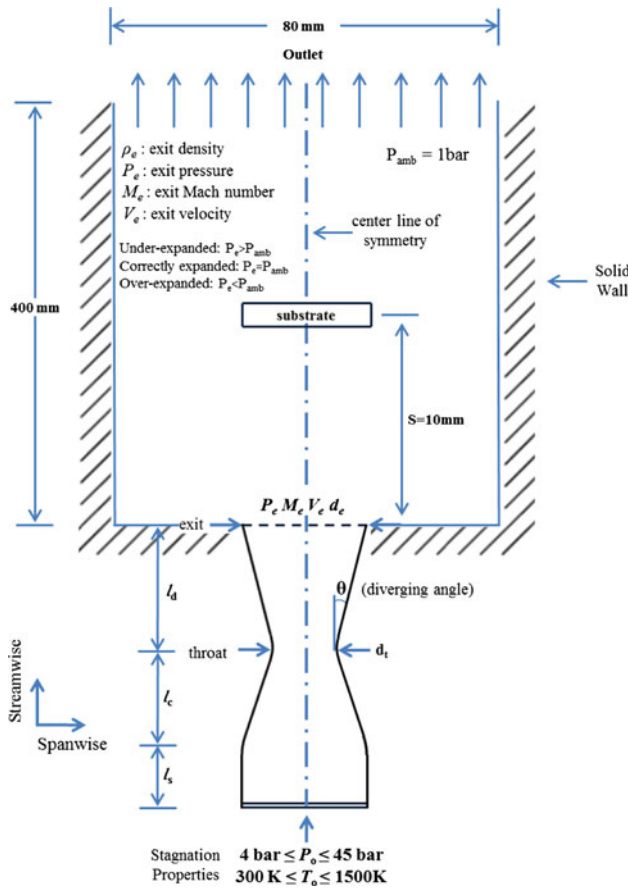


**Fig. 1** A schematic of *de Laval* converging-diverging nozzle. The nozzle stagnation pressure and temperature ranges are  $4 \leq P_0 \leq 45$  bar and  $300 \leq T_0 \leq 1500$  K. No particles are injected; only the supersonic flow characteristics are examined. A line of symmetry bisects the nozzle in the spanwise direction to cut the computational cost in half. Depending on the nozzle geometry, ( $l_d$ ,  $l_c$ ,  $l_s$ ,  $d_e$ ,  $d_t$ ), flow characteristics change, as manifest in under-, correctly-, and over-expanded nozzles

In general, optimal operating conditions are defined as functions of particle impact speed and temperature. Particle speed (in addition to its diameter and density) determines its impact momentum and energy. If the impact energy is too low, then particles do not adhere to the substrate and can end up eroding the substrate causing foreign-object damage (FOD). If particle momentum is excessive, then FOD again occurs, but to an even greater extent. Particle temperature is also an important factor because it influences particle “hardness” (or brittleness or ductility). If the particle temperature is too low, the particle may be too brittle to flatten or mollify for deposition. Conversely, if the particle temperature is too high, then the particle may be too ductile to be fractured—some degree of brittleness is desired for efficient deposition. Figure 2 shows the window of scalability (Ref 18) defined between the curves of erosion (i.e.,  $V_{eros}$ ) and critical velocity (i.e.,  $V_{crit}$ ). The critical velocity is defined as the minimum velocity needed for deposition. To ensure deposition efficiency (i.e., the ratio of the weight of deposited material to the net weight of the feed material),

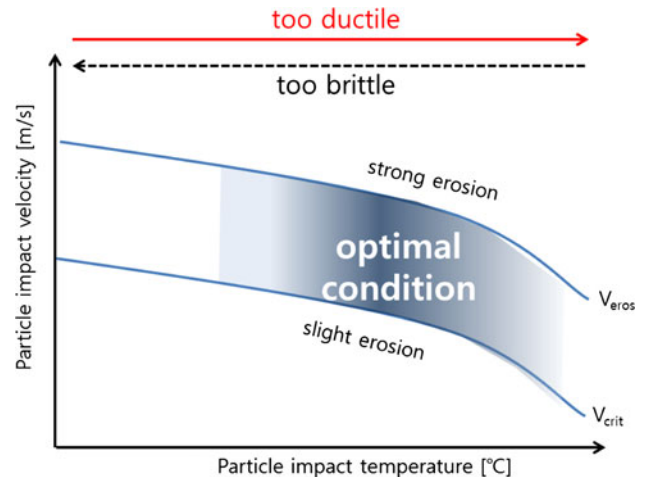


**Fig. 2** The optimal operating condition in terms of particle impact velocity and temperature. If the particle temperature is too low and high, then the particle is too brittle and ductile, respectively. If the particle velocity is too low and high, then the particle momentum (or impact energy) is too low and high, respectively, both of which result in erosion of the substrate

particle temperatures should also remain within the window of scalability.

Another primary factor influencing the supersonic flow in particle coating is the nozzle geometry. There is a maximum Mach number, established by the nozzle geometry; regardless of how high the operating pressure and temperature go, the maximum Mach number is constrained by the nozzle geometry. If a higher Mach number is preferred, then the diverging section of the nozzle must be further expanded. However, over-expansion may allow surrounding (ambient) air to infiltrate the nozzle (because of low static and stagnation pressure at the nozzle exit), thereby adversely affecting flow. Such a flow would have decreased flow velocities as momentum is dissipated through unwanted shocks. Across shocks, the Mach number and velocity decrease, but the density, entropy, static pressure, and temperature of the gas increase. Enthalpy (or stagnation temperature) may be conserved, but momentum (or stagnation pressure) decreases because of friction. This article quantitatively estimates the *momentum loss to friction* (referred to as “ $p$ -loss” or “loss in  $P_0$ ”) for various nozzle geometries. Additional  $p$ -losses induced by shocks and jet relaxation by entrained ambient air are considered.

The coating method studied here is actually a mixture of both cold-spray and aerosol-deposition techniques; it is similar to cold-spray technology in that it is a non-vacuum coating technology, but it also has characteristics of aerosol-deposition (Ref 19) because it uses fine powders (i.e., a few hundreds nanometer that can fit through the small nozzle throat). Four different nozzle configurations are studied. The diverging section of each nozzle is variable while the throat size is constant. All 2D Navier-Stokes computations of fully viscous flow are carried out for atmospheric pressure of  $P_{amb} = 1$  bar with air as the working fluid. Frictional  $p$ -losses from the

nozzle to the substrate were estimated as the stagnation pressure was increased from  $P_o=4-45$  bar at fixed  $T_o=300$  K. Additional computations study the effect of varying  $T_o$  at fixed  $P_o=20$  bar. The  $p$ -losses for these cases are estimated as a function of the cases' initial  $P_o$  and  $T_o$ . Also, exit static pressures, temperatures, and velocities are recorded and compared with the isentropic solutions. Any scenario that deviates from the correctly expanded (or shock-free) condition of  $P_e=P_{amb}=1$  bar yields a diamond shock structure. In this study, the correctly expanded (shock-free) condition refers to  $P_e=P_{amb}$  (where losses due to shock waves and shear interactions are minimized).

## 2. Modeling Descriptions

### 2.1 Governing Equations

The CFD computations solve the nonlinear, compressible Navier-Stokes (NS) equations (Fluent 6.3), thereby accounting for shockwaves, turbulence, and viscous dissipation effects of the working fluid (i.e., air). The second-order-accurate computations are performed on a 2D domain, which is consistent with the actual 2D slot-type nozzle used in experiments (Ref 7, 19). Of course, even a rectangular slot-type nozzle has some 3D flow characteristics (Ref 20). The 2D flow assumption could fail under the following two cases: (1) First, the 2D flow assumption fails when the depth of the slot nozzle in

the  $z$ -direction is insufficient and yields 3D “hairpin” vortices (Ref 21-24). (2) Second, the 2D assumption fails at relatively low Reynolds or Mach numbers when the viscous boundary layer leads to 3D azimuthal instability and eventually to turbulence. On the other hand, at relatively high Reynolds or Mach numbers, boundary-layer effects can be neglected (i.e., it is nearly an inviscid flow). In our studies, the Mach number is fairly high (i.e.,  $M > 0.6$ ), and the 2D flow assumption is well within the regime of validity. In addition, 2D simulations are *an-order-of-magnitude* less expensive in terms of the computational cost and, thus, it is more attractive than 3D simulations.

The governing equations for continuity, momentum, energy, and re-normalized group (RNG)  $k$ - $\varepsilon$  turbulence equations in Einsteinian notation are as follows:

$$\text{Continuity equation: } \frac{\partial}{\partial x_i}(\rho u_i) = 0 \quad (\text{Eq 1})$$

$$\text{Momentum equation: } \frac{\partial}{\partial x_i}(\rho u_i u_j) = -\frac{\partial P}{\partial x_i} + \frac{\partial \tau_{ij}}{\partial x_i} \quad (\text{Eq 2})$$

$$\text{Equation of state: } \rho = \frac{P_o + P}{(R_u/M_w)T} \quad (\text{Eq 3})$$

$$\text{Energy equation: } \frac{\partial \rho e u_i}{\partial x_i} = -\frac{\partial p u_i}{\partial x_i} + \frac{\partial (u_j \tau_{ij} - q_i)}{\partial x_i} \quad (\text{Eq 4})$$

$k$ - $\varepsilon$  turbulence equation:

**Table 1 Detailed dimensions for Nozzles 1, 2, and 3**

Nozzle	Substrate	$S$ , mm	$l_s$ , mm	$l_c$ , mm	$l_d$ , mm	$d_c$ , mm	$d_e$ , mm	$\theta$ , °
0	With	10	10	10	10	0.4	1.50	3.72
1	Without	NA	10	10	10	0.4	0.56	0.47
2		NA	10	10	10	0.4	0.70	0.86
3		NA	10	10	5	0.4	1.45	5.98

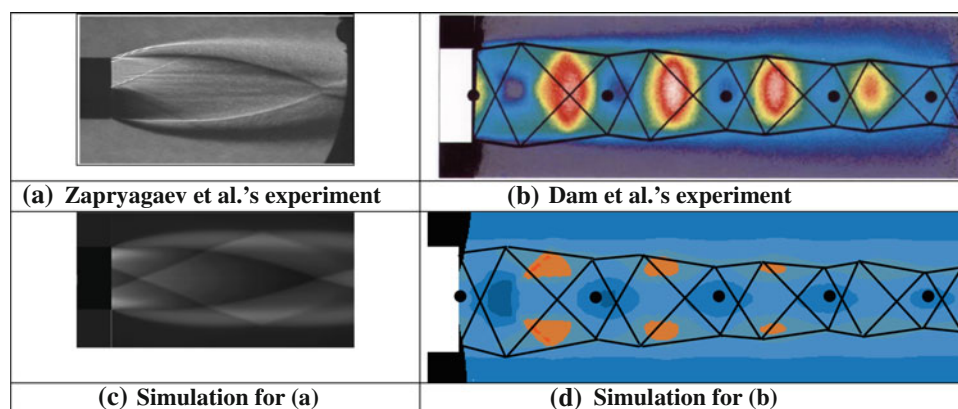


**Fig. 3** Qualitative comparisons between experiments and our simulations of a supersonic, non-isobaric gas jet for the under-expanded nozzle. (a) Details for the Zapryagaev et al. (Ref 27) nozzle: a conical nozzle with a  $15^\circ$  half-angle at  $M=3$ . The nozzle exit inner and outer diameters are 30 and 32 mm, respectively. The nozzle exit pressure is  $n=P_e/P_{mb}=2.3$ . (b) Generation of diamond shockwaves exiting from Dam et al.'s (Ref 28) under-expanded nozzle. The snapshot is taken on the time scale of the duration of the laser pulse (18 ns). The nozzle stagnation pressure is 3 bar. Lines indicate shock and expansion waves while dots represent the density maxima

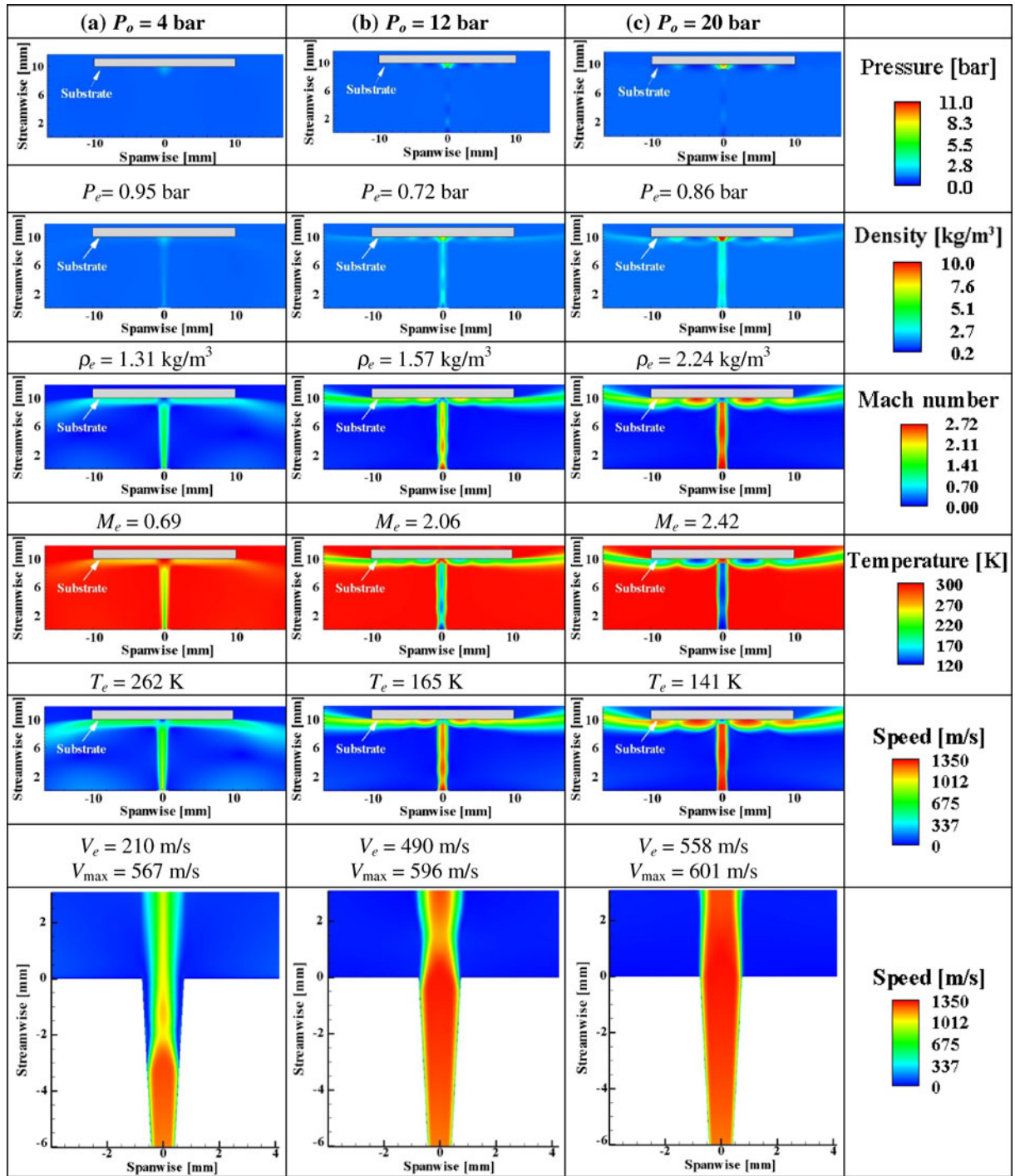


**Fig. 4** Effect of stagnation pressure ( $P_o = 4, 12,$  and  $20$  bar) on flow characteristics at  $T_o = 300$  K

$$\frac{\partial \rho k u_i}{\partial x_i} = \frac{\partial}{\partial x_j} \left( \alpha_k \mu_{\text{eff}} \frac{\partial k}{\partial x_j} \right) + \mu_t S^2 - \rho \epsilon \left( 1 - 2 \sqrt{\frac{k}{a^2}} \right)$$

$$\frac{\partial \rho \epsilon u_i}{\partial x_i} = \frac{\partial}{\partial x_j} \left( \alpha_\epsilon \mu_{\text{eff}} \frac{\partial \epsilon}{\partial x_j} \right) + C_{1\epsilon} \frac{\epsilon}{k} \mu_t S^2$$

$$- \rho \frac{\epsilon^2}{k} \left[ C_{2\epsilon} + \frac{C_{\mu} \rho \eta^3 (1 - \eta/\eta_0)}{1 + \beta \eta^3} \right] \mu_t = \frac{\rho C_{\mu} k^2}{\epsilon} \quad (\text{Eq 5})$$

where  $\rho$ ,  $u$ ,  $P$ ,  $T$ ,  $e$ ,  $\tau$ ,  $q$ ,  $R_u$ , and  $M_w$  are the gas density, velocity, pressure, temperature, internal energy, viscous shear stress, heat flux, universal gas constant, and molecular weight, respectively.  $P$  is the local, static, or ambient pressure, and  $P_o$  is the operating or stagnation pressure applied at the nozzle inlet. The Mach number is  $M = u/a$ , where  $a = (\gamma R_u T / M_w)^{1/2}$ , and  $\gamma$  is the specific heat ratio.

Further details on the numerical procedures and algorithms are available in the Fluent manual (Ref 25).

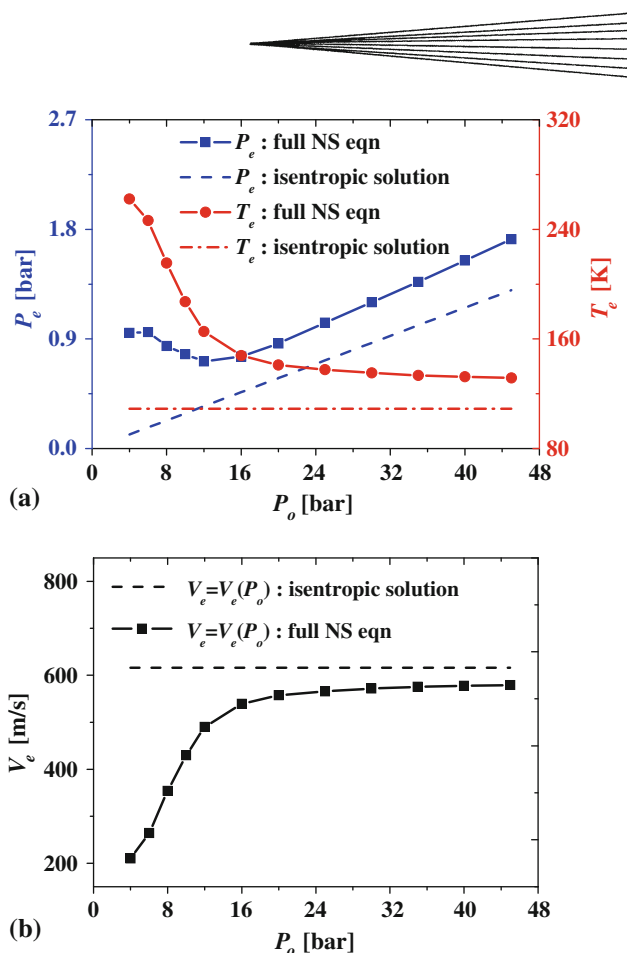
## 2.2 Numerical Details

Figure 2 is a schematic of the supersonic nozzle used in this study. Gas properties at the nozzle exit and the upstream stagnation point are denoted by “e” and “o” subscript, respectively. Also, subscripts “c” and “d” refer to converging and diverging sections of the nozzle, respectively. The surrounding or ambient pressure,  $P_{amb}$ , is set to 1 bar. The standoff distance between the nozzle exit and the substrate is labeled “S,” fixed at 10 mm.

For computations *with* a substrate, 48,250 nodes ( $50 \times 300 = 15,000$  for the nozzle and  $175 \times 190 = 33,250$  for the external domain) are used. Nearly 26,250 nodes are used for the region between the nozzle exit and the substrate, and nearly 7,000 nodes are used for the region downstream of (behind) the substrate. Minimum grid spacing is  $\Delta x = 0.0008$  mm, which is sufficient to capture the dominant frequency of convective flow as well as the Kolmogorov length scale. Grid sensitivity studies confirmed that the numerical solution is not contingent upon grid resolution when the total number of nodes exceeds about 25,000. No-slip Dirichlet boundary condition are applied along all walls while the Neumann boundary condition is used for the outlet. The spanwise dimension of the computational domain is sufficiently so large (relative to the nozzle dimensions) that the side walls have little effect on the supersonic flow near the nozzle center. No-slip boundaries are imposed at the side walls in all computational runs. The Neumann boundary condition at the substrate wall specifies a zero-gradient temperature. The nozzle is assumed to be perfectly insulated, and subjected to a no-heat-flux boundary condition. A frictionless line of symmetry bisects the spanwise direction and cuts the computational cost in half. The physical dimension of the computational domain is  $80 \times 400$  mm<sup>2</sup>. Stagnation pressure ranges from  $P_o = 4$ -45 bar. The working fluid is air, whose temperature ranges from  $T_o = 300$ -1500 K. Table 1 describes the nozzle (Nozzle 0) used in this case.

Additional computations are carried out *without* a substrate (Nozzle 1, 2, and 3). 102,000 nodes ( $60 \times 600 = 36,000$  for the nozzle and  $220 \times 300 = 66,000$  for the external domain) are used. Minimum grid spacing is  $\Delta x = 0.0023$  mm. For these simulations, various nozzle geometries are investigated as described in Table 1.

Simulations were carried out for supersonic gas flow only, without consideration of particles. Particle impact velocity can be estimated through use of the Stokes number ( $Stk$ ). It is safe to assume that the particle velocity is 70-90% of the gas velocity if  $Stk < 0.2$ . This assumption implies that the particle response time is small and there is little slip between particle and gas (Ref 26).



**Fig. 5** Comparison between the isentropic flow (analytic) and the fully viscous flow (2D NS equation) solutions as a function of the stagnation pressure,  $P_o$ . (a) Flow static pressure and temperature at the nozzle exit. (b) Flow exit velocity ( $V_e$ ) as a function of  $P_o$ .

## 3. Results and Discussion

### 3.1 Validation

Figure 3(a) and (b) show Schlieren and UV-laser-Rayleigh-scattering images, respectively, of a supersonic non-isobaric gas jets from an under-expanded nozzle. The pressure ratio is  $P_e/P_{amb} = 2.3$  for the Schlieren image from Zapryagaev et al. (Ref 27) in Fig. 3(a). The UV-laser-Rayleigh-scattering images from Dam et al. (Ref 28) in Fig. 3(b) shows four periodic diamond structures within 26 mm downstream; the white rectangle is the nozzle exit. Our axisymmetric model of the Dam et al. experiment in Fig. 3(d) correctly approximates the frequency of the diamond shockwaves. The diamond shockwaves dissipate downstream both in the experimental image and in our simulation. Moreover, the model correctly predicts the expansion of the jet downstream. It should be noted that Fig. 3(c) and (d) are obtained on the basis of the axisymmetric (i.e.,  $z$ - $r$  axes) simulations while all other computational runs are based on the 2D (i.e.,  $x$ - $y$ ) model.

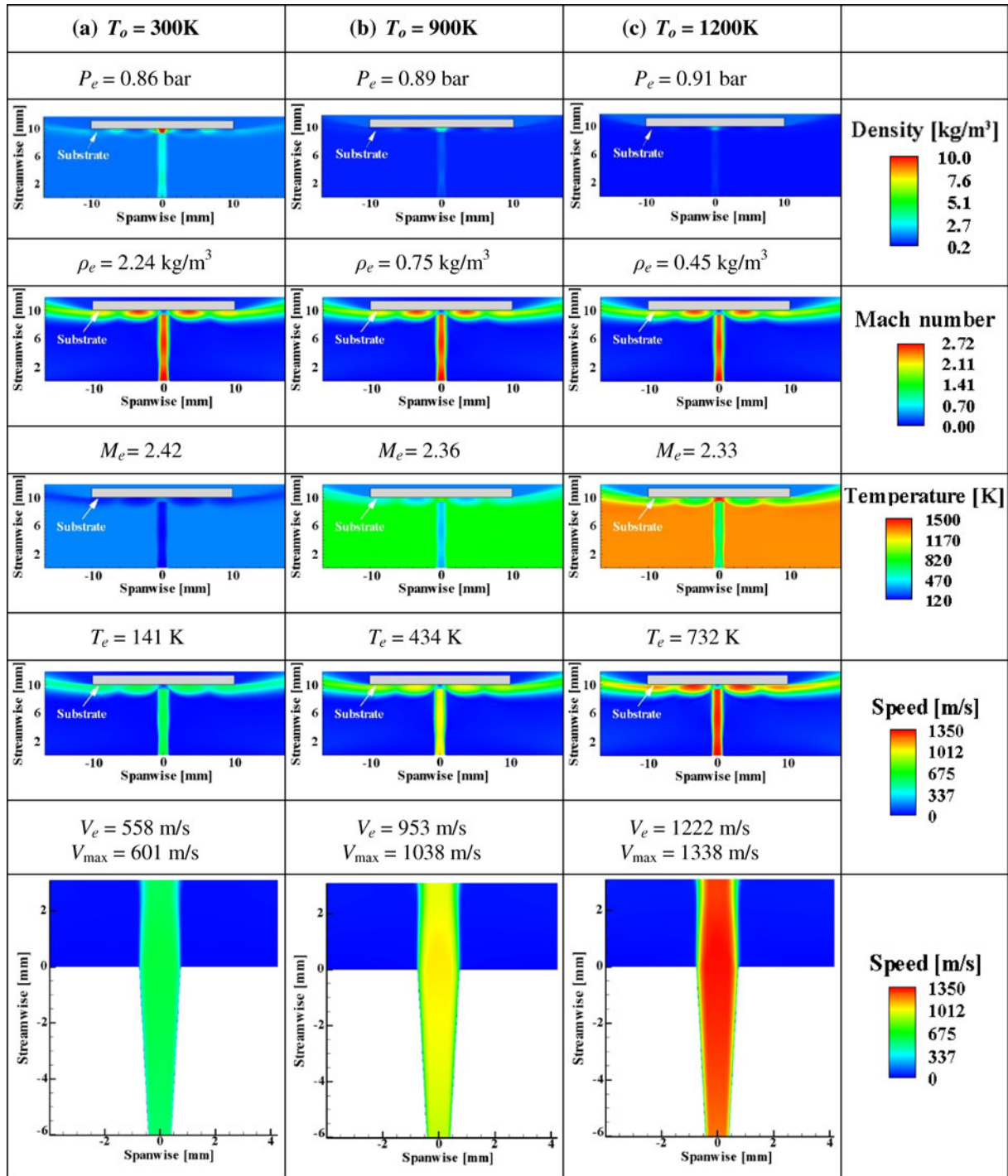


**Fig. 6** Effect of stagnation temperature ( $T_o = 300, 900, \text{ and } 1500 \text{ K}$ ) on flow characteristics at  $P_o = 20 \text{ bar}$

### 3.2 Effect of Stagnation Properties on Jet Impingement

Figure 4 shows the effect of  $P_o$  on flow characteristics (pressure, density, Mach number, static temperature, and speed) at  $T_o = 300 \text{ K}$ . Exit properties are obtained by averaging over the exit plane. Because the nozzle geom-

etry is fixed (see Table 1), the maximum Mach number at the nozzle exit is  $M_e = 2.96$ . This also constrains the exit static temperature and velocity to  $T_e = T_o / (1 + 0.2M_e^2) = 109 \text{ K}$  and  $V_e = \sqrt{2c_p T_o [1 - (P_e/P_o)^{(\gamma-1)/\gamma}]} = M_e^2 \sqrt{\gamma R T_e} = 619 \text{ m/s}$ , respectively. The ratio of stagnation

to static pressure is also limited to  $P_o/P_e = (1 + 0.2M_e^2)^{3.5} = 34.6$ . All of these analytic values are applicable only to a 1D, isentropic flow. The snapshots of Fig. 4 illustrate interesting flow characteristics both inside the nozzle and near the substrate. At a low stagnation pressure ( $P_o = 4$  bar), ambient pressure infiltrates the nozzle and actually reverses the flow near the nozzle wall. Furthermore, the jet rapidly loses momentum because of low  $P_o$ . On the other hand, at  $P_o = 20$  bar, momentum is largely sustained. Moreover, the stagnation density at the substrate is about  $\rho_o = 10$  kg/m<sup>3</sup> (half of the initial value of  $\rho_o = 20$  kg/m<sup>3</sup>), implying that the stagnation pressure is also reduced by half according to the ideal gas law  $P_o = \rho_o RT_o = 10$  bar. The stagnation temperature remains near 300 K, while only about half of the stagnation pressure is recovered at the substrate (Ref 29).

In the 2D, full NS viscous flow solutions, the exit static pressure ( $P_e$ ), temperature ( $T_e$ ), and velocity ( $V_e$ ) deviate significantly from the isentropic solution at lower  $P_o$ , as shown in Fig. 5(a) and (b), respectively. However, the 2D, NS velocity results approach the isentropic solution at higher  $P_o$ , when the viscous forces in the supersonic flow are proportionally smaller, as in Fig. 5(b). This trend implies that losses are minimized at higher operating pressures within the nozzle because of decreased relative viscous forces.

Figure 6 shows the effect of  $T_o$  on flow characteristics at fixed  $P_o = 20$  bar. The same nozzle as in Fig. 4 yields an exit Mach number of  $M_e = 2.96$  and pressure ratio of  $P_o/P_e = (1 + 0.2M_e^2)^{3.5} = 34.6$  (hence,  $P_e = 0.58$  bar that corresponds to  $P_o = 20$  bar). The isentropic exit temperature and velocity shown in Fig. 7 are computed as  $T_e = T_o / (1 + 0.2M_e^2)$  and  $V_e = M_e \sqrt{\gamma RT_e}$ . These isentropic exit properties are compared to their fully viscous NS solution counterparts in Fig. 7. The isentropic exit pressure is relatively low (i.e., 0.58 bar from Fig. 7a) because velocity is increased by nozzle expansion which reduces the static pressure. Also, the NS solution indicates that the static pressure reduction (or velocity increase) is less influential than the isentropic process because of losses induced by shocks and viscous dissipation. Static temperature also drops as thermal energy is converted into kinetic energy. Thus, a significant temperature drop is a good indicator of efficient flow acceleration. The isentropic static temperature at the nozzle exit is lower than that of the full NS solution, indicating that, of course, the temperature reduction (or flow acceleration) is more efficient when the flow is isentropic. Figure 7(b) also indicates that the real velocities are lower than isentropic velocities because of losses to shocks and viscous dissipation. With increasing  $T_o$ , velocity differences are magnified because of increased loss to thermal and viscous dissipation and shocks.

The loss in  $P_o$  as a function of  $P_o$  and  $T_o$  is quantified in Fig. 8, which summarizes all computational runs from Fig. 3-6 (identical conditions). Recall that  $p$ -loss is the percentage difference between  $P_o$  (nozzle inlet) and the final stagnated pressure measured at the substrate, which

indicates how much  $P_o$  is decreased through shocks and viscous dissipation. The  $p$ -loss is roughly constant at about 55% and is not strongly dependent upon  $T_o$  for constant

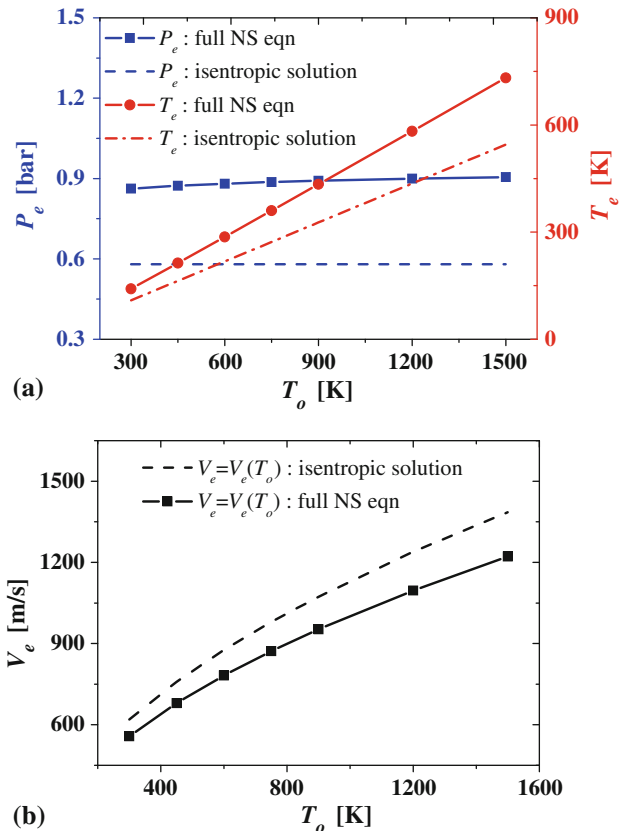


**Fig. 7** Comparison between the isentropic flow (analytic) and the fully viscous flow (2D NS equation) as a function of the stagnation temperature,  $T_o$ . (a) Flow static pressure and temperature at the nozzle exit. (b) Flow exit velocity ( $V_e$ ) as a function of  $T_o$ .

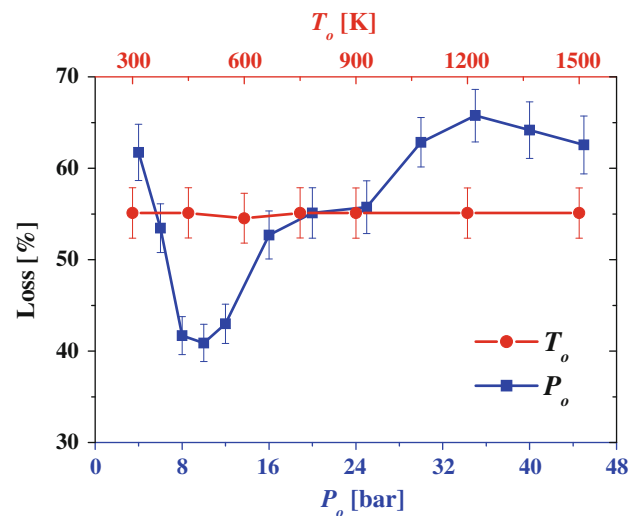


**Fig. 8** The total loss in stagnation pressure as a function of  $P_o$  or  $T_o$ .

$P_o = 20$  bar. Although temperature differences are reflected in the varied gas velocity (as in Fig. 7b), it does not significantly impact exit pressures, which are not temperature dependent as shown in Fig. 7(a). Because there is little

change in shock structures upon varying  $T_o$ ,  $p$ -loss also changes little as shown in Fig. 8 (see the line with circles).

The shape of the curve illustrates, first, the effects of viscous dissipation between the streaming jet and

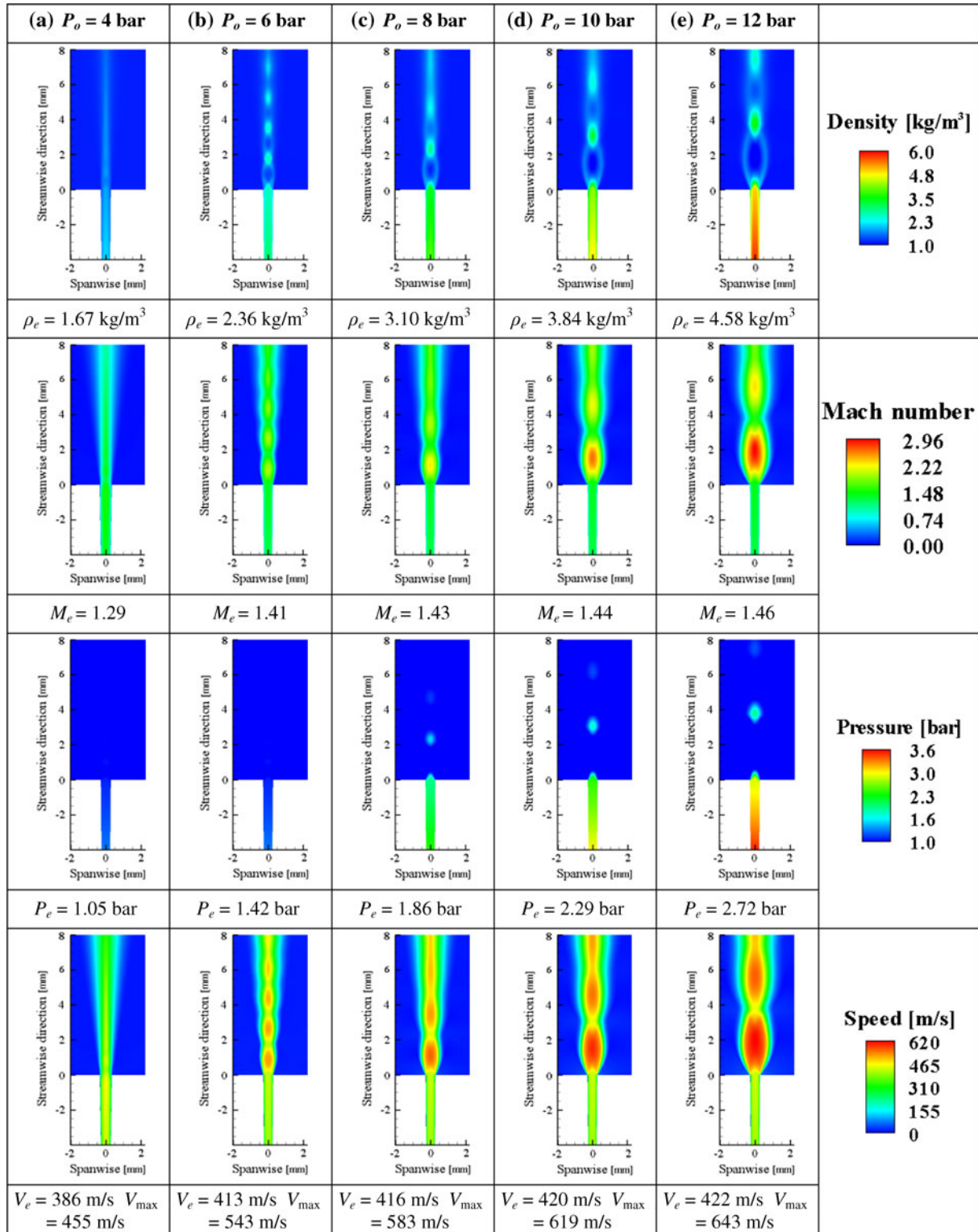


**Fig. 9** Under-expanded nozzle (Nozzle 1): effect of stagnation pressure ( $P_o = 4, 6, 8, 10,$  and  $12$  bar) on flow characteristics at  $T_o = 300$  K

surrounding air and then the effects of shocks. The  $p$ -loss is minimum near  $P_o = 10$  bar and reaches a near-steady value of 65% at  $P_o = 30$  bar.

The snapshots of Fig. 6 also illustrate some interesting physics of compressible flow. Figure 8 shows that there is about a 55% loss in  $P_o$  regardless of  $T_o$  (gas pressure at the substrate is about 9 bar for all  $T_o$ ). Based on the ideal gas law ( $P_o = \rho_o RT_o$ ), density must be varied inversely with  $T_o$  to maintain constant pressure. The density snapshots reveal exactly this; density decreases with increasing  $T_o$ . From the viewpoint of particle coating, this density decrease near the substrate is favorable because drag decreases (particle speed is maintained). Another feature in Fig. 6 is that the Mach number snapshots are fairly constant across all cases. Noting that  $T = T_o/(1 + 0.2M^2)$  and considering the corresponding temperature snapshots ( $T$  increases with  $T_o$  at fixed  $M$ ), the overall jet velocity increases because  $V_e = M\sqrt{\gamma RT}$  ( $T$  increases with  $T_o$  at fixed  $M$ ). Overall, the jet structure is not particularly sensitive to  $T_o$  (see Fig. 6) although  $P_o$  clearly affects the jet structure (see Fig. 4).

### 3.3 Flow Characteristics of Various Nozzles

In this section, the effects of various nozzle geometries on flow characteristic are studied. Three nozzles (Nozzles 1, 2, and 3 from Table 1) are configured: under- (i.e.,  $P_e > P_{amb}$ ), near-correctly (actually, *slightly* under-), and over-expanded (i.e.,  $P_e < P_{amb}$ ) nozzles. When the nozzle

is under-expanded, the pressure inside the nozzle is too high; the nozzle should have been expanded further to reduce the pressure and thereby increase the exit velocity. For an over-expanded nozzle, pressure inside the nozzle is low, and this low pressure can lead to separated or reversed flow inside. It should have been less expanded (or  $P_o$  increased) to obtain an ambient exit pressure (Ref 30)

Snapshots in Fig. 9 compare the jet structures and flow properties for Nozzle 1 as a function of  $P_o$ . With increasing  $P_o$ , the density, pressure, and velocity at the nozzle exit increase. Exit Mach number variation is minimal because it is fixed by the nozzle geometry. Downstream variations in Mach number with  $P_o$  are observed; increasing  $P_o$  yields shock diamonds with longer wavelengths. Corresponding velocity variations are observed as gas decelerates across a shock. The shock structures dissipate downstream through viscous damping. According to Fig. 5(b), the isentropic exit velocity is  $V_e = \sqrt{2c_p T_o [1 - (P_e/P_o)^{(\gamma-1)/\gamma}]} = 619$  m/s ( $T_o = 300$  K and  $P_e/P_o = 1/34.6$  are fixed). In the fully viscous NS simulations, the exit velocity varies slightly between  $385 < V_e < 422$  m/s, which is significantly lower than the isentropic velocity of 619 m/s.

Figure 10 shows how centerline flow characteristics vary with  $P_o$  for Nozzle 1. Both density (Fig. 10a) and pressure (Fig. 10b) decrease significantly at the nozzle throat and continue to do so during flow expansion in the diverging section. For Nozzle 1 (under-expanded) at

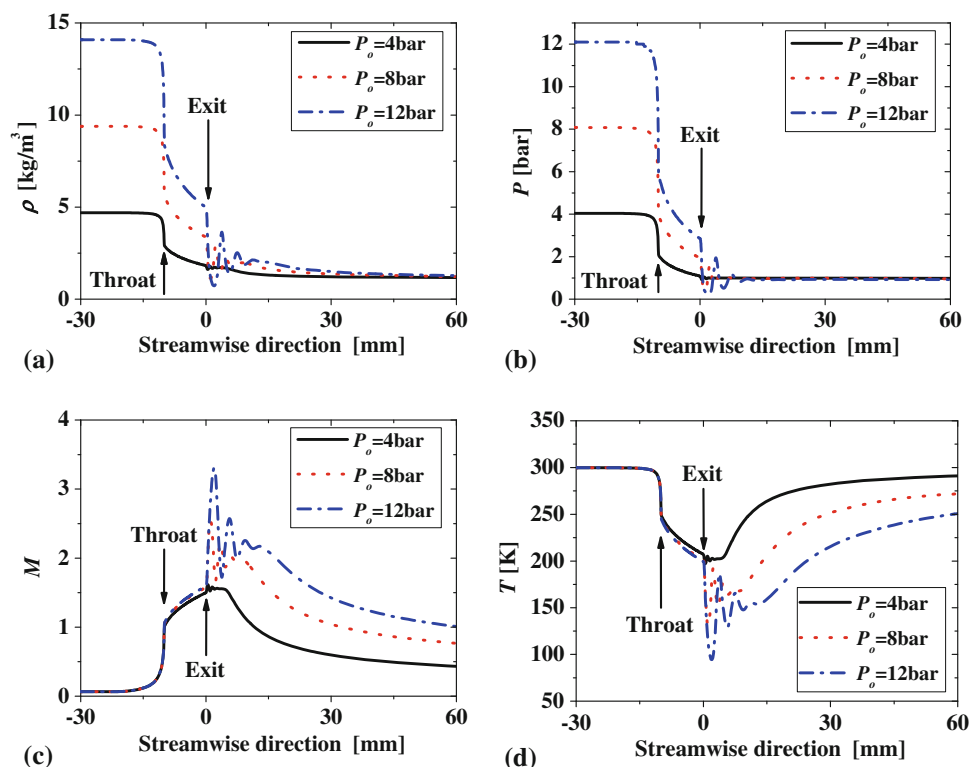


**Fig. 10** Variations of (a) gas density, (b) pressure, (c) Mach number, and (d) temperature in the streamwise direction, both inside and outside the under-expanded nozzle (Nozzle 1)

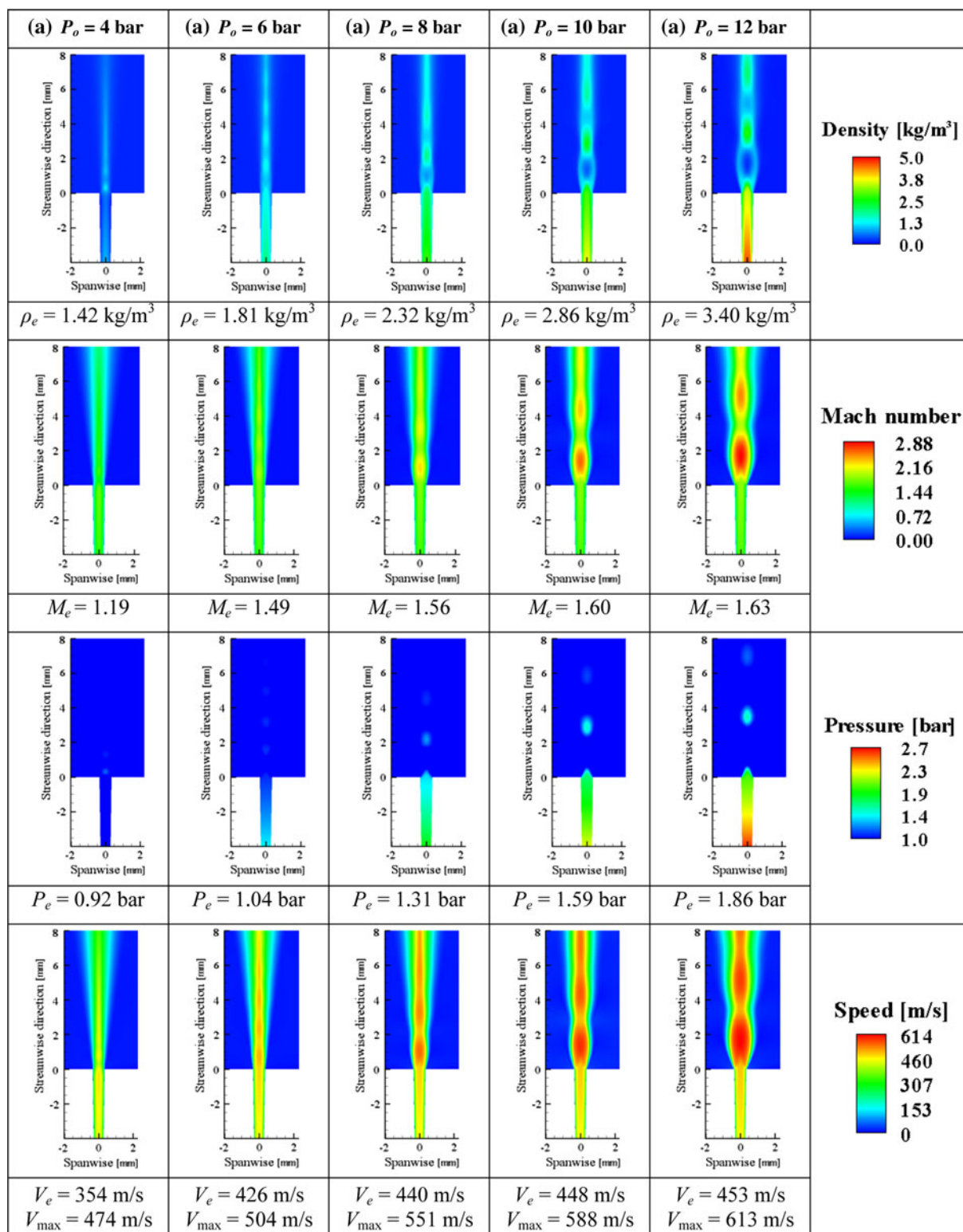


**Fig. 11** Nearly *correctly* expanded (or shock-free) nozzle (Nozzle 2): Effect of stagnation pressure ( $P_o = 4, 6, 8, 10,$  and  $12$  bar) on flow characteristics at  $T_o = 300$  K

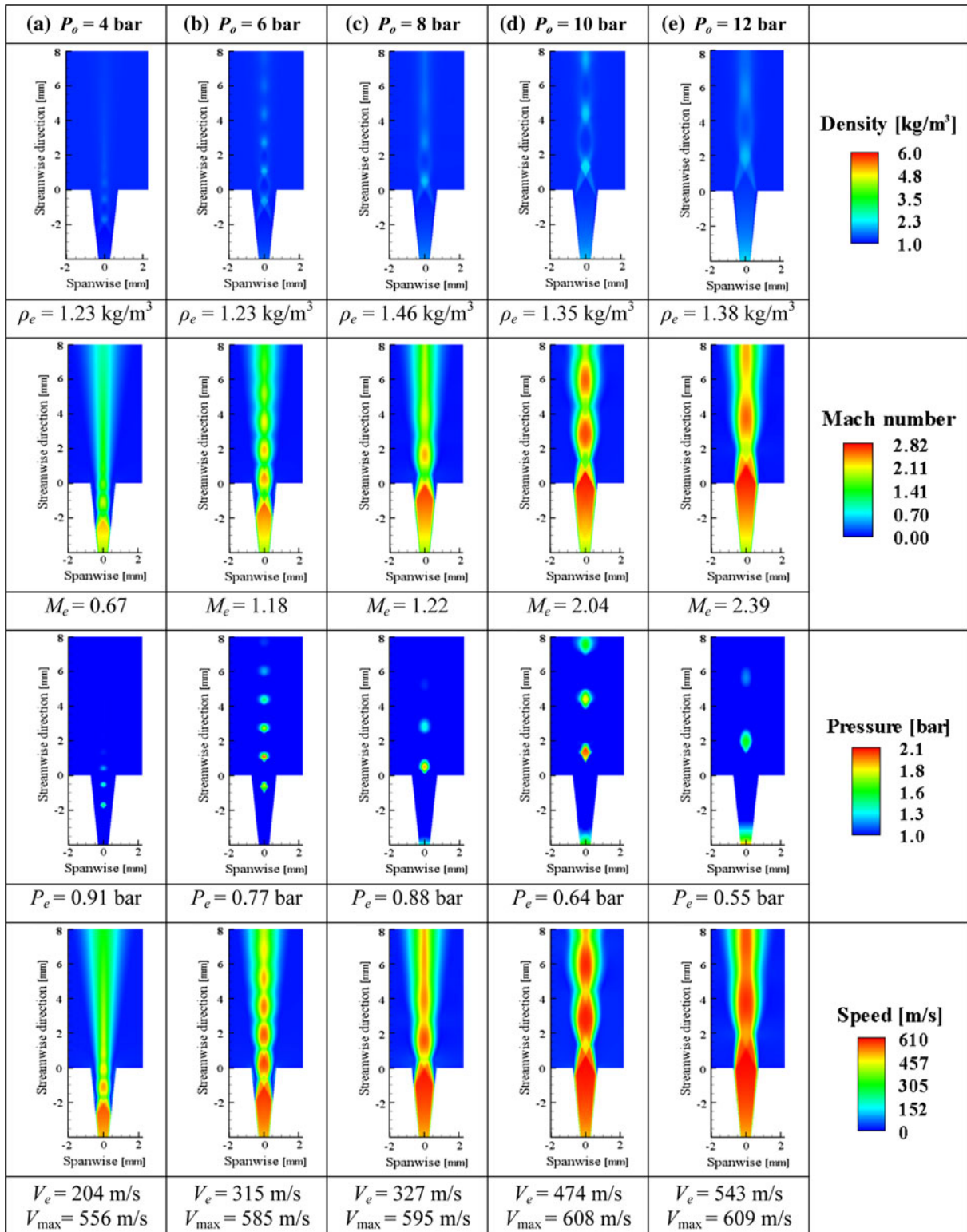
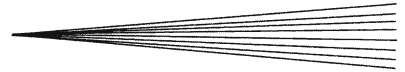


**Fig. 12** Over-expanded nozzle (Nozzle 3): Effect of stagnation pressure ( $P_o = 4, 6, 8, 10,$  and  $12$  bar) on flow characteristics at  $T_o = 300$  K

$P_o=4$  bar, there is minimal shock (see Fig. 9a). Slight fluctuations in density and pressure in Fig. 10(a) and (b) also indicate *weak* shockwaves. Pressure quickly equilibrates with the ambient air at 1 atm. As shown in Fig. 10(c) and (d), Mach number increases and temperature decreases at the throat and downstream of the expansion. For larger  $P_o$  (8 and 12 bar), both  $M$  and  $T$  fluctuate significantly across the shocks. Neither  $M$  nor  $T$  reaches the ambient air pressure by 60 mm downstream.

Figure 11 shows snapshots of density, Mach number, pressure, and speed at various  $P_o$  for Nozzle 2, which is *slightly* under-expanded (see Table 1) and, thus requires a slightly larger  $P_o$  to yield  $P_e=P_{amb}$ . As expected, it requires  $P_o=6$  bar (as opposed to 4 bar for Nozzle 1) to yield  $P_e=1.04$  bar; see Fig. 11(b). Shockwaves are still apparent even at  $P_e=1.04$  bar because of the 4% pressure difference (only at  $P_e=1$  bar should no shocks formed). This proves that shock formation is very sensitive to pressure differences. Because Nozzle 2 is only *slightly* under-expanded compared to Nozzle 1, Mach number increases, and, hence, the exit velocity increases. The diamond shock structure is much less prominent in the jet.

In Fig. 12, the nozzle is further expanded, requiring a much larger  $P_o$  to fill the nozzle's diverging section with high momentum gas. When  $P_o$  is low (4 bar) as in Fig. 12(a), a separated (even reversed) flow occurs at the nozzle wall. Increasing  $P_o$  fills the nozzle with high momentum gas (see the speed contours), and eventually the region of separated flow disappears. The exit pressure is  $P_e=0.55$  bar at  $P_o=12$  bar, which indicates that even high  $P_o$  does not completely stop flow infiltration. Diamond shock structures are clearly evident in all panels of Fig. 12.

Figure 13 compares nozzle exit pressures under varied  $P_o$ . Nozzle 1 is under-expanded even at the lowest  $P_o$  of 4 bar because the exit pressure is slightly larger than  $P_{amb}=1$  bar. This under-expanded nozzle is to be avoided because it requires  $P_o < 4$  bar to meet  $P_e < P_{amb}$ . This

low value of  $P_o$  yields low gas exit speeds that do not allow for particle coating. Nozzle 2 is acceptable for  $4 < P_o < 12$  bar. At the moderate value of  $P_o=6$  bar, the correctly expanded (shock-free) condition of  $P_e=P_{amb}$  is met. However, even Nozzle 2 may not yield sufficiently high gas speeds; the nozzle must be expanded even further to accelerate the flow. Nozzle 3, although over-expanded, would yield sufficiently high gas speeds if provided sufficient  $P_o$ . Figure 13 shows that the range of  $P_o$  considered herein is still not sufficiently high to make good use of the over-expanded nozzle;  $P_o$  needs to be significantly increased to reach the state of  $P_o=P_{amb}$ .

## 4. Conclusion

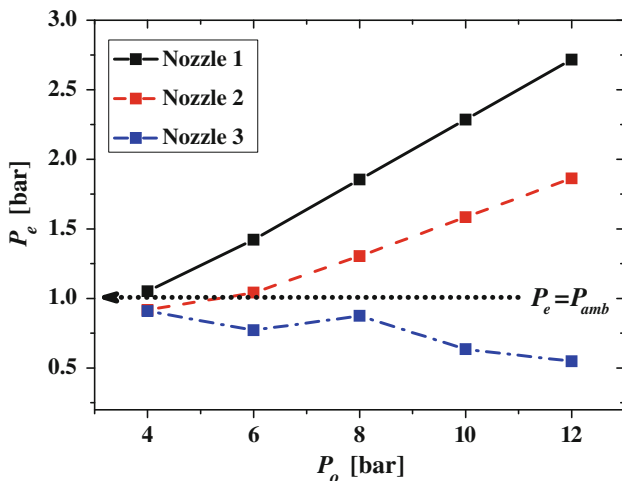
A turbulent flow model was applied to investigate the characteristics of supersonic flow for low-temperature particle coating applications. A supersonic nozzle was simulated for various ranges of stagnation pressures and temperatures ( $4 < P_o < 45$  bar and  $300 < T_o < 1500$  K). Ranges of the exiting Mach number and velocity are  $0.6 < M_e < 3.5$  and  $200 < V_e < 1400$  m/s, respectively. The energy loss through shockwaves and shear interactions between the streaming jet and surrounding gas are quantified as a function of  $P_o$  and  $T_o$ . Jets demonstrate 40-60% friction-induced decrease in  $P_o$  regardless of  $T_o$ . Nozzle designers and operators should keep in mind that to yield a nozzle exit condition of  $P_e=P_{amb}$ ,  $P_o$  should be adjusted rather than  $T_o$  as  $T_o$  has little effect on exit pressures. On the other hand,  $T_o$  is more influential than  $P_o$  at varying exit velocities. Supersonic flows for three nozzles (under-, *slightly* under-, and over-expanded) were simulated and their correctly expanded (or shock-free) operating conditions were identified. Diamond shock structures induced by a pressure imbalance between the exiting gas and the surrounding atmosphere were captured.

## Acknowledgments

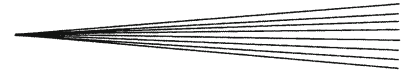
This study was supported by the New & Renewable Energy Program through the Korea Institute of Energy Technology Evaluation and Planning (KETEP, 2010-3010010011) grant and Technology Innovation Program (KETEP, 10035397-2010-01). The corresponding author also acknowledges that a partial support was made for this project by the NRF Grant of Korea (2010-0010217 and 2011-0007182).

## References

1. R.C. Dykhuizen, M.F. Smith, D.L. Gilmore, R.A. Neiser, X. Jiang, and S. Sampath, Impact of High Velocity Cold Spray Particles, *J. Therm. Spray Tech.*, 1999, **8**(4), p 559-564
2. A.P. Alkhimov, S.V. Klinkov, V.F. Kosarev, and A.N. Papyrin, Gas-Dynamic Spraying Study of a Plane Supersonic Two-Phase Jet, *J. Appl. Mech. Tech. Phys.*, 2007, **38**(2), p 324-330



**Fig. 13** Static pressure at the nozzle exit at various stagnation pressures for Nozzles 1, 2, and 3



3. D.L. Gilmore, R.C. Dykhuizen, R.A. Neiser, M.F. Smith, and T.J. Roemer, Particle Velocity and Deposition Efficiency in the Cold Spray Process, *J. Therm. Spray Tech.*, 1999, **8**(4), p 576-582
4. T.H. Van Steenkiste, J.R. Smith, and R.E. Teets, Aluminum Coatings via Kinetic Spray with Relatively Large Powder Particles, *Surf. Coat. Technol.*, 2002, **154**(2-3), p 237-252
5. J.A. Hearley, J.A. Little, and A.J. Sturgeon, The Effect of Spray Parameters on the Properties of High Velocity Oxy-Fuel NiAl Intermetallic Coatings, *Surf. Coat. Technol.*, 2000, **123**, p 210-218
6. L. Ajdelsztajn, B. Jodoin, G.E. Kim, and J.M. Schoenung, Cold Spray Deposition of Nanocrystalline Aluminum Alloys, *Metall. Mater. Trans. A*, 2005, **36A**, p 657-666
7. J. Akedo, Room Temperature Impact Consolidation (RTIC) of Fine Ceramic Powder by Aerosol Deposition Method and Applications to Microdevices, *J. Therm. Spray Tech.*, 2008, **17**(2), p 181-198
8. B. Jodoin, Cold Spray Nozzle Mach Number Limitation, *J. Therm. Spray Tech.*, 2002, **11**(4), p 496-507
9. A.P. Alkhimov, S.V. Klkinkov, V.F. Kosarev, and A.N. Papyrin, Gas-Dynamic Spraying Study of a Plane Supersonic Two-Phase Jet, *J. Appl. Mech. Technol. Phys.*, 1997, **38**(2), p 324-330
10. A.P. Alkhimov, V.F. Kosarev, and A.N. Papyrin, Method of Cold Gas Dynamic Spraying, *Sov. Phys. Dokl.*, 1990, **35**(12), p 1047-1049
11. H. Assadi, F. Gartner, T. Stoltenhoff, and H. Kreye, Bonding Mechanism in Cold Gas Spraying, *Acta Mater.*, 2003, **51**, p 4379-4394
12. J. Vlcek, H. Huber, H. Voggenreiter, A. Fischer, E. Lugscheider, and H. Hallen, Kinetic Powder Compaction Applying the Cold Spray Process A Study on Parameters, *ITSC Proc.*, 2001, p 417-422
13. C.J. Li and W.Y. Li, Deposition Characteristics of Titanium Coating in Cold Spraying, *Surf. Coat. Technol.*, 2003, **167**(2-3), p 278-283
14. R.C. Dykhuizen and R.A. Neiser, *ITSC Proc.*, 2003, p 19-26
15. W.Y. Li and C.J. Li, Optimal Design of a Novel Cold Spray Gun Nozzle at a Limited Space, *J. Therm. Spray Tech.*, 2005, **14**(3), p 391-396
16. B. Samareh and A. Dolatabadi, A Three-Dimensional Analysis of the Cold Spray Process: The Effects of Substrate Location and Shape, *J. Therm. Spray Tech.*, 2007, **16**(5-6), p 634-642
17. H. Takana, K. Ogawa, T. Shoji, and H. Nishiyama, Computational Simulation of Cold Spray Process Assisted by Electrostatic Force, *Powder Technol.*, 2008, **185**(116-123), p 116-123
18. T. Schmidt, F. Gartner, H. Assadi, and H. Kreye, Development of a Generalized Parameter Window For Cold Spray Deposition, *Acta Mater.*, 2006, **54**, p 729-742
19. J. Akedo, Aerosol Deposition of Ceramic Thick Films at Room Temperature: Densification Mechanism of Ceramic Layers, *J. Am. Ceram. Soc.*, 2006, **89**(6), p 1834-1839
20. F.F. Grinstein, Vortex Dynamics and Entrainment in Rectangular Free Jets, *J. Fluid Mech.*, 2001, **437**, p 69-101
21. M.T. Landahl, Wave Mechanics of Breakdown, *J. Fluid Mech.*, 1972, **56**, p 775-802
22. T. Herbert, Secondary Instability of Boundary Layers, *Annu. Rev. Fluid Mech.*, 1988, **20**, p 487-526
23. B.J. Bayly, S.A. Orszag, and T. Herbert, Instability Mechanisms in Shear-Flow Transition, *Annu. Rev. Fluid Mech.*, 1988, **20**, p 359-391
24. K. Itoh, Y. Nakamura, and Y. Kukita, Free-Surface Shear Layer Instabilities on a High-Speed Liquid Jet, *Fusion Technol.*, 2000, **37**, p 74-88
25. F.U.s. Guide, *Fluent User's Guide*, 2008
26. W.Y. Li, C.-J. Liu, C.X. Wang, and H.S. Bang, Measurement and Numerical Simulation of Particle Velocity in Cold Spraying, *J. Therm. Spray Tech.*, 2006, **15**(4), p 559-562
27. V.I. Zapryagaev, A.N. Kudryavsev, A.V. Lokotok, A.V. Solotchin, A.A. Pavlov, and A. Hadjadj, An Experimental and Numerical Study of a Supersonic-Jet-Shock-Wave Structure, *Proceedings of the XI International Conference on the Methods of Aerophysical Research*, Vol 2, 2002, p 187-191
28. N.J. Dam, M. Rodenburg, R.A.L. Tolboom, G.G.M. Stoffels, P.M. Huisman-Kleinherenbrink, and J.J. ter Meulen, Imaging of an Underexpanded Nozzle Flow by UV Laser Rayleigh Scattering, *Exp. Fluids*, 1998, **24**(2), p 93-101
29. J.D. Anderson and J. David, *Computational Fluid Dynamics*, McGraw-Hill, 1995
30. J.J. Park, M.W. Lee, S.S. Yoon, H.Y. Kim, S.C. James, S.D. Heister, S. Chandra, W.H. Yoon, D.S. Park, and J.H. Ryu, Supersonic Nozzle Flow Simulations for Particle Coating Applications: Effects of Shockwaves, Nozzle Geometry, Chamber Pressure, and Substrate Location Upon Flow Characteristics, *J. Therm. Spray Tech.*, 2010, p 1-9